Optical Properties of Neutral F Centers in Bulk MgO with Density Matrix Embedding

Shreya Verma,[†] Abhishek Mitra,[†] Yu Jin,[†] Soumi Haldar,[†] Christian Vorwerk,[‡] Matthew R. Hermes,[†] Giulia Galli,[*,‡,†,¶] and Laura Gagliardi[*,†,‡,§]

[†]*Department of Chemistry, University of Chicago, Chicago, Illinois 60637, United States*

[‡]*Pritzker School of Molecular Engineering, University of Chicago, Chicago, Illinois 60637, United States*

[¶]*Materials Science Division and Center for Molecular Engineering, Argonne National Laboratory, Lemont, Illinois 60439, United States*

[§]*Argonne National Laboratory 9700 S. Cass Avenue Lemont, Illinois 60439, United States*

E-mail: gagalli@uchicago.edu; lgagliardi@uchicago.edu

Abstract

The optical spectra of neutral oxygen vacancies (F^0 centers) in the bulk MgO lattice was investigated using density matrix embedding theory. The impurity Hamiltonian was solved with the complete active space self-consistent field (CAS-DMET) and second-order n-electron valence state perturbation theory (NEVPT2-DMET) multireference methods. To estimate defect-localized vertical excitation energies at the non-embedding and thermodynamic limits, a double extrapolation scheme was employed. The extrapolated NEVPT2-DMET vertical excitation energy value of 5.24 eV agrees well with the experimental absorption maxima at 5.03 eV, whereas the excitation energy value of 2.89 eV at the relaxed triplet defect localized state geometry overestimates the experimental emission at 2.4 eV by only nearly 0.5 eV, indicating the involvement of triplet-singlet decay pathway.

Introduction

F centers are point defects commonly observed in metal oxides, arising from anion vacancies. They possess distinct electronic states, including a singlet ground state and a triplet excited state. The optical properties of the F centers are highly tunable, making them suitable for a wide range of color-center laser applications.[1] In particular, magnesium oxide (MgO), an ionic oxide, exhibits F centers that significantly influence the material's chemical properties, thus making it a promising candidate for optoelectronic and catalytic applications.[2,3] The interesting properties of F centers in alkaline earth oxides can be attributed to their distinct electronic structure which results from the emergence of new local energy levels within their optical gap. F centers can trap one or two electrons within the anion vacancy, resulting in the formation of F^+ and F^0 centers respectively. The electrostatic stabilization effectively retains these electrons within the vacancy due to the large Madelung constant of the ionic crystal.[4]

In this study, we focus specifically on the neutral oxygen vacancy, the F^0 center in the bulk of MgO crystal, and aim to understand the optical transitions involved. The F^0 center in MgO has been extensively investigated. The optical absorption energy has been computed using quantum chemical embedded cluster approaches,[5,6] periodic boundary conditions using equation of motion coupled cluster theory,[7] quantum Monte Carlo[8] and many-body perturbation theory methods.[9,10] Despite their seemingly simple nature, MgO F^0 centers are electronically complex, and there is disagreement between the molecular quantum chemical and solid-state calculations on the nature of the electronic states involved in the optical absorption and emission spectra. The absorption maxima has been experimentally determined to occur at 5.03 eV.[11] The absorption process involving the midgap state can occur in two ways: (i) an electron is promoted to the conduction band minimum (CBM), known in literature as photoionization, or (ii) defect localized excitation to one of the higher energy triply degenerate states. Quasiparticle excitation methods[9] and quantum Monte Carlo studies[8] have suggested that the absorption maxima is due to the photoionization process, with the

exception of the recent embedded-BSE study.[12] On the other hand, wave-function based methods have always attributed the absorption maxima to the defect localized excitation.[2,7] A report by Rosenblatt et al.[13] measures a difference of 0.06 eV between the relaxed F^0 center excited state and the conduction band edge, suggesting that the two processes are energetically similar. Overall, there is an uncertainty of the states involved in the absorption process. The experimental emission bands have been detected at around 2.4 eV and 3.1 eV.[13,14] The later has been ascribed to the F^0 center, interpreted to arise from a singlet-singlet, triplet-singlet transition,[15] recombination of midgap electrons with the valence holes[9] or hole capture at an F^+ center.[12] However, there is no definitive evidence that establishes which transitions correspond to the photoluminescence bands. The lack of a fundamental understanding engenders the need to seek a method which can affordably deliver an accurate quantum chemical description of the electronic interplay in MgO F^0 center.

Furthermore, F^0 centers have degeneracy in the low-lying defect localized excited states, giving rise to strong electronic correlation. Computing electronic excitation energies in extended systems is still a challenge for *ab initio* quantum chemistry methods. Although density functional theory is commonly employed for periodic calculations,[16] its single determinant nature is inadequate for addressing multireference systems.[17] This is the reason one needs multireference quantum chemistry methods or the inclusion of many body effects through the Green's function method,[18] to explore multiconfigurational systems, despite their steep computational scaling. Fortunately, strong correlation in point defect materials tends to be localized, implying that uniform accuracy throughout the quantum chemical model may not be necessary.

Recently, quantum embedding methods have emerged as efficient approaches for calculating optical transitions involving strongly correlated electrons. These methods involve mapping the infinite bulk system onto an impurity model embedded within a bath.[19–23] By partitioning the full system into smaller fragments, these techniques address the computational complexity associated with extended systems featuring localized correlation. The

fragment with the region of interest is treated with an expensive yet accurate method and is embedded in the rest of the system termed as the environment, which is solved at a low cost, mean field level of theory. Various quantum embedding theories have been reported in the literature[19,24,25] leveraging the different central embedding variable. These variables include the density,[26–29] the density matrix[30,31] and the Green's function.[32–37] In this study, we employ the periodic version of density matrix embedding theory (pDMET).[20,23,30,38,39] Due to the localized nature of strongly correlated defects, such as F centers in MgO, they are well-suited for embedding methods.

Density Matrix Embedding Theory

Optical transitions for bulk F^0 center have been studied utilizing the periodic-DMET algorithm[38] with complete active space self-consistent field (CASSCF) and second-order N-electron valence state perturbation theory (NEVPT2) high-level impurity solvers.[20] For a more thorough understanding of the DMET framework, we refer the readers to the available extensive literature.[30,31,38–46] Briefly, the algorithm begins with a Slater determinant trial wave function that approximates the entire system. It can be a restricted closed-shell Hartree Fock (RHF) or restricted open-shell Hartree Fock (ROHF) wave function. Subsequently, all orbitals (N_{tot} in number) are transformed into maximally localized Wannier functions (MLWFs) and divided into N_{frag} number of fragment and the remainder environment MLWFs, based on the specific system being investigated. By performing a singular value decomposition (Schmidt decomposition)[47] on the fragment-environment block of the full one-body reduced density matrix, a set of bath orbitals is generated as a linear combination of environment MLWFs that are entangled with the fragment MLWFs. By using a RHF (ROHF) Slater determinant trial wave function, there will be a maximum of N_{frag} (N_{frag}+2S) bath orbitals,[20] where S represents the total spin quantum number of the periodic supercell. To solve the DMET embedding Hamiltonian, multiconfigurational methods

such as CASSCF and NEVPT2 are employed.

Computational Methods

The DMET calculations were carried out using the pDMET code developed in our group,[48,49] which utilizes electron integrals and quantum chemistry solvers from PySCF.[50,51] Wannierization was performed with the wannier90[52] program through the pyWannier90 interface.[53] Geometry optimizations were performed with periodic boundary conditions at the gamma point, at the PBE level, using Quantum Espresso.[54,55] In order to allow the localization of electrons within the cavity, a set of Gaussian basis functions was placed at the vacancy site. We used four defective supercells in this work- three primitive supercells ($2 \times 2 \times 2$, $3 \times 3 \times 3$, $4 \times 4 \times 4$) with 15, 53 and 127 atoms, respectively, and one conventional $2 \times 2 \times 2$ supercell with 63 atoms (Figure 1). The pseudopotential of Goedecker, Teter and Hutter (GTH)[56,57] was used along with a combination of double- and triple-zeta valence polarized Gaussian basis sets consistent with this pseudopotential for all calculations. The description of basis sets and other computational details are provided in the Supporting Information. Geometry optimization in excited states was carried out using time-dependent density functional theory (TDDFT) method within the Tamm-Dancoff approximation, as implemented in the WEST code.[58–60] The equilibrium atomic geometries of excited states were obtained by minimizing the nuclear forces below the threshold of 0.01 eV/Å. CAS-DMET calculations for singlet-singlet excitations are performed using the CAS (2e, 5o) with a state average over five states with equal weights. For singlet-triplet excitations, state average over five singlet and four triplet states is used with the same active space and equal weight on each of the nine states.

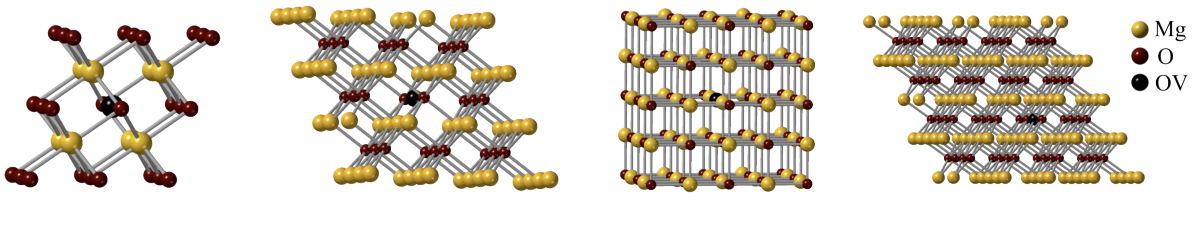

Figure 1: The four different supercells involved in the periodic DMET study along with their nomenclature and the respective number of atoms in each.

Results and Discussion

The pristine cubic MgO crystal exhibits octahedral (O_h) symmetry. The nearest pair of magnesium (Mg) atoms are 4.26 Å apart in the PBE-optimized geometry. Upon removing an oxygen atom, the resulting vacancy retains the original symmetry, but the two electrons trapped in the vacancy cause a slight outward shift (0.04 Å) of the six closest magnesium (Mg) atoms surrounding the oxygen vacancy (OV). This defect generates an occupied totally symmetric (a_{1g}) s-type single-electron state within the band gap as well as a set of three unoccupied p-type atomic orbital states (t_{1u}) above the conduction band (Figure 2). Both

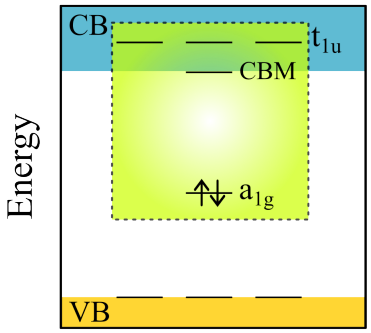

Figure 2: Qualitative single-electron energies: the midgap singlet state orbital a_{1g} and defect localized unoccupied orbitals t_{1u} are labeled. The green box identifies the complete active space.

singlet and triplet excitations, specifically, $^1A_{1g} \rightarrow {}^1T_{1u}$ and $^1A_{1g} \rightarrow {}^3T_{1u}$, have been examined. The presence of a triply degenerate excited state necessitates a multiconfigurational

approach to handle static correlation effectively, followed by multireference perturbation theory to capture dynamical correlation. Hereby, in our DMET calculations, the CASSCF solver (CAS-DMET) is employed to account for static correlation and the NEVPT2 solver (NEVPT2-DMET) captures dynamic correlation.

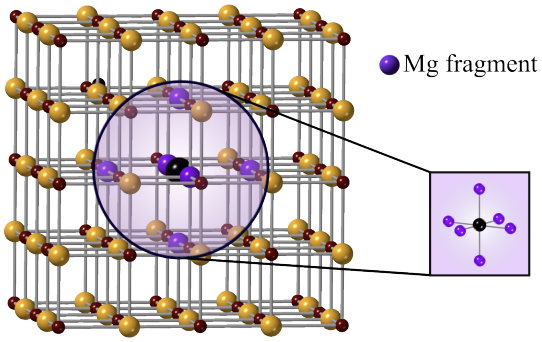

Figure 3: The face centered cubic MgO crystal with the DMET fragment cluster ($OV-Mg_6$) consisting of the nearest neighbor 6 Mg atoms around the vacancy.

Once the DMET embedding space (consisting of fragment and bath orbitals) is generated through the ROHF trial wave function, we define the complete active space (CAS) with two active electrons in five active orbitals (2e,5o), shown in Figure 4 below. This includes the defect localized a_{1g} and three degenerate t_{1u} orbitals, along with the CBM orbital. The CASSCF impurity ground state wave function is dominated by the $a_{1g}^{\uparrow\downarrow}$ determinant. The CAS selected here is larger than the minimal active space of (2e,2o), previously used in symmetry-constrained cluster calculations.[5,6] The use of periodic boundary conditions facilitates the straightforward treatment of delocalized CBM-like orbitals because of the absence of spurious boundary effects.

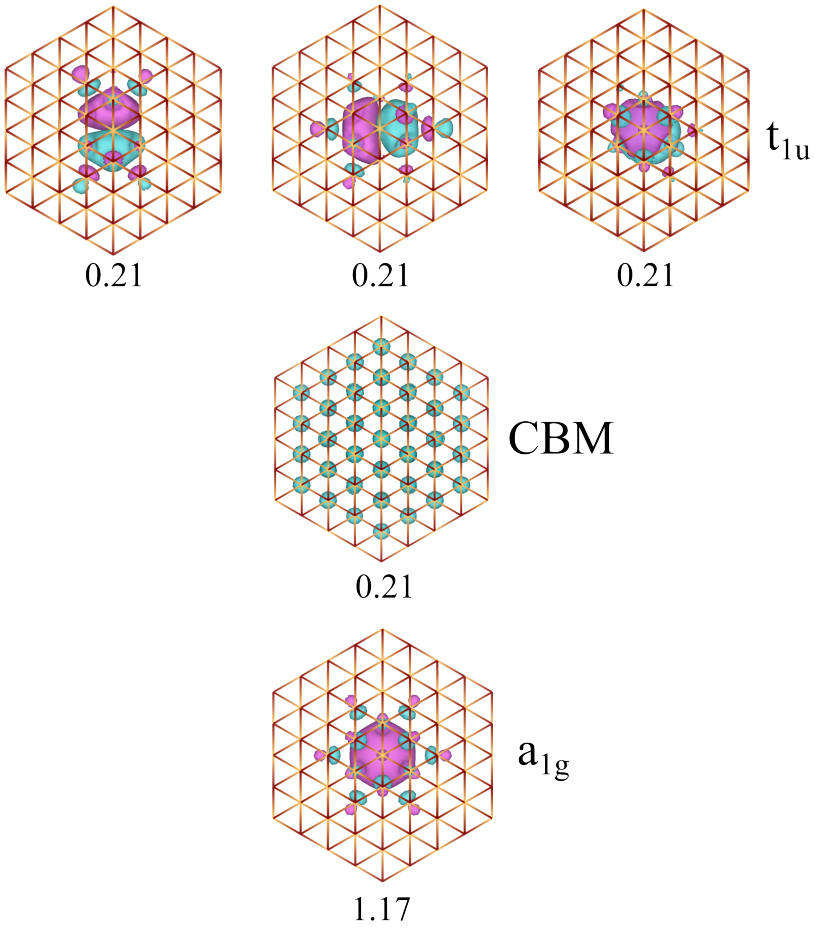

Figure 4: The CAS-DMET natural orbitals for (2e,5o) active space. The orbitals are centered on the vacancy. The numbers below the orbitals are the state-averaged occupation numbers, with a state average over five states.

Scrutinizing the CAS-DMET active space, our optimized CBM orbital has no inversion center, meaning the photoionization process is dipole forbidden, since the ground state is closed-shell. In case delocalized orbitals with an inversion center were available at higher energies, we also checked a (2e,8o) CAS. No delocalized states with u-symmetry in the targeted energy range were obtained. Therefore, our initial goal is to compute the energy difference between $^1A_{1g}$ and $^1T_{1u}$ states. Figure 5 shows the linear trend of CAS-DMET and NEVPT2-DMET excitation energies with embedding size, for each supercell, for the local singlet transition ($^1A_{1g}\rightarrow{}^1T_{1u}$) and for the excitation to the delocalized state associated to the CBM ($^1A_{1g}\rightarrow{}^1CBM$).

To compute these vertical excitation energies (VEEs), we vary the number of embedding orbitals (N_{emb}), which includes both the fragment and bath orbitals. The initial step involves adjusting N_{emb} in the fragment OV$-$Mg$_6$ of a supercell, illustrated in Figure 3. For each DMET calculation, the number of fragment orbitals (N_{frag}) is selected from the MLWFs located within a specified distance, r_{frag}, from the initial OV$-$Mg$_6$ fragment. The corresponding N_{frag}+2 entangled bath orbitals are included to obtain the N_{emb}. Following this procedure, DMET excitation energies are calculated for different values of N_{frag}, by gradually increasing r_{frag}. This strategy is applied to each of the four supercells. In principle, N_{frag} can be increased only up to (N_{tot}-2)/2 in case of a ROHF bath. Here N_{tot} is the total number of atomic orbitals or total number of MLWFs for a particular supercell. However, the location of the DMET fragment itself in the computational supercell is also crucial to dictate the maximum N_{frag} (or r_{frag}) that will be physically meaningful. The distance r_{frag} should not exceed the distance of the fragment atoms from the atoms on the supercell boundary to avoid spurious interactions with periodic images, which can lead to specious trends in DMET VEEs. Additionally, the case where $N_{\mathrm{tot}}/N_{\mathrm{emb}}$=1, is the non-embedding limit VEEs calculated through DMET.

A linear decrease in the computed VEEs with increasing N_{emb} is observed. Consequently, it is possible to extrapolate the VEEs to the non-embedding limit, the values of which are reported in Table 1.

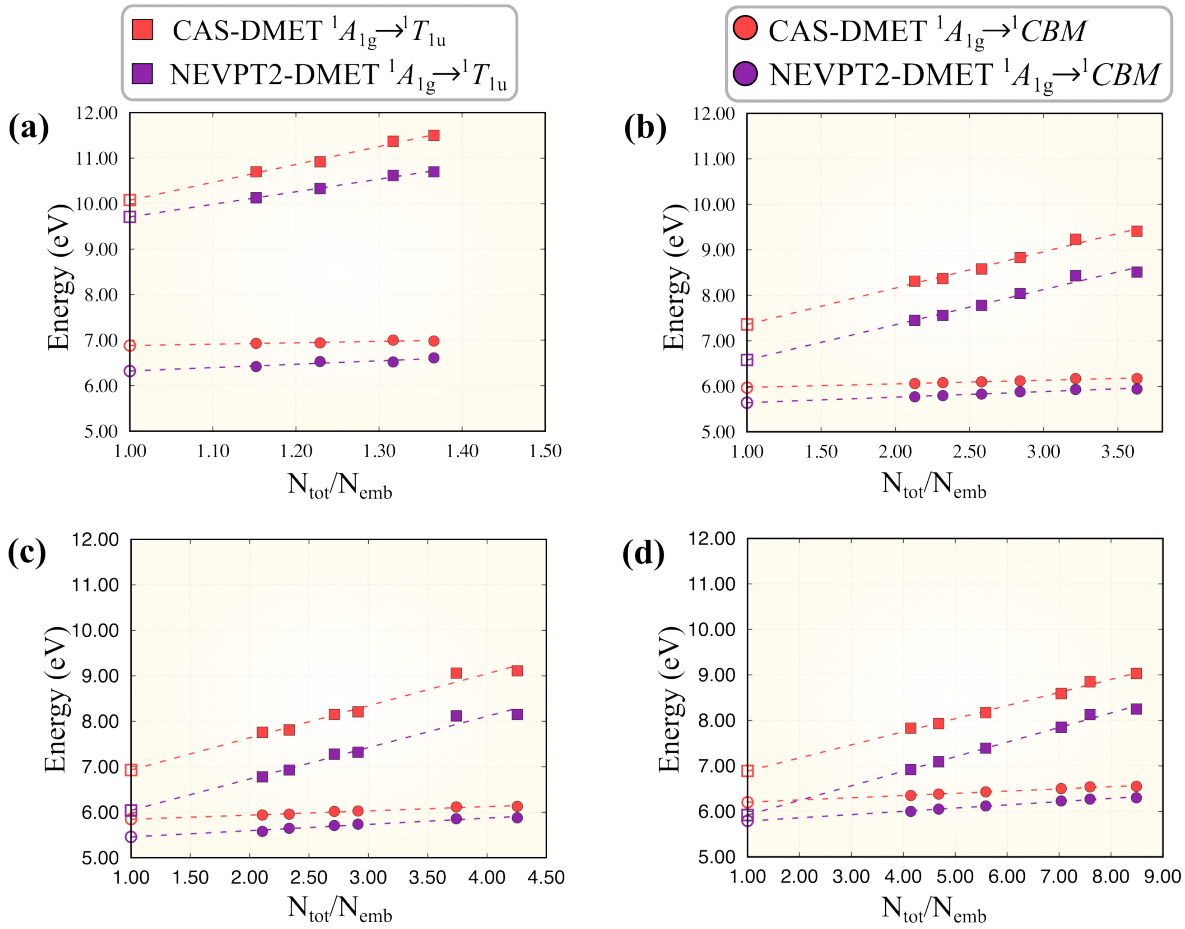

Figure 5: Extrapolation of CAS-DMET and NEVPT2-DMET excitation energies for the two transitions ($^1A_{1g}\rightarrow{}^1T_{1u}$ and $^1A_{1g}\rightarrow{}^1CBM$) to the non-embedding limit for supercells (a) primitive $2\times2\times2$, (b) primitive $3\times3\times3$ (c) conventional $2\times2\times2$ and (d) primitive $4\times4\times4$. The solid squares (circles) represent DMET data points for the singlet excitations to t_{1u} (CBM) and the hollow squares and circles denote the respective extrapolated VEEs. The red (purple) color symbolizes CAS-DMET (NEVPT2-DMET).

Let us now discuss the photoionization. We aim to understand how a 'local' embedding framework handles an electronic transition involving a 'delocalized' state. The CAS-DMET and NEVPT2-DMET VEEs for this excitation from A_{1g} to CBM are plotted in Figure 5.

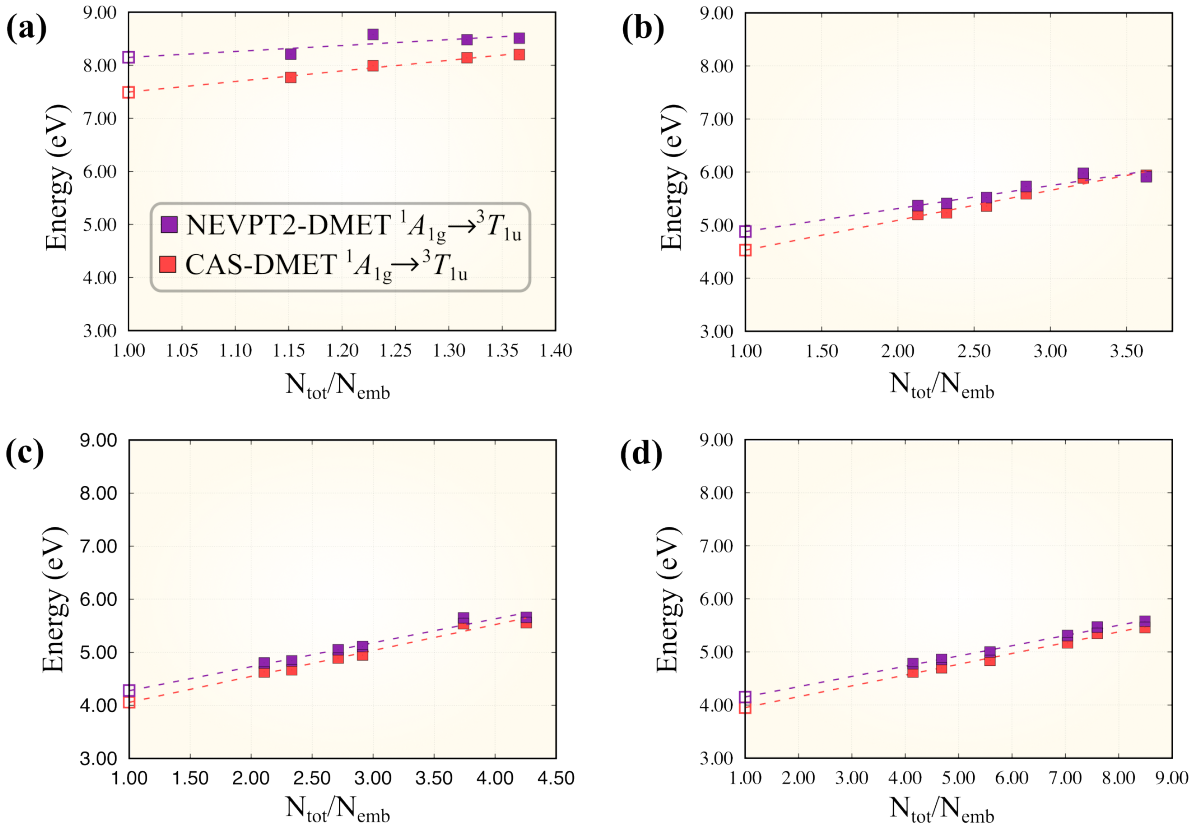

Figure 6: Extrapolation of CAS-DMET and NEVPT2-DMET excitation energies ($^1A_{1g}\rightarrow{}^3T_{1u}$) to the non-embedding limit for primitive supercells (a) $2\times2\times2$, (b) $3\times3\times3$ (d) $4\times4\times4$ and (c) conventional cell $2\times2\times2$. The solid squares represent DMET data points and the hollow squares denote extrapolated energy values.

Next, we examine the singlet-triplet transition of the F^0 center. Experimentally, there are two peaks in the emission spectra at 2.3 eV and 3.2 eV, attributed to the F^0 and F^+ centers, respectively.[13] Since the lifetime of the F^0 photoluminescence is longer, it has been suggested that the emission occurs through a triplet to singlet transition.[6,7,12,61] Therefore, we first show in Figure 6 the VEEs from the singlet a_{1g} ground state to the triplet t_{1u} state, following the same procedure of varying embedding space described above for singlet-singlet transitions. The difference between CAS-DMET and NEVPT2-DMET values is less compared to the analogous singlet-singlet transition. This implies a lower degree of dynamic correlation for the triplet excited states.

Since the objective is to calculate the deexcitation energy from the relaxed $^3T_{1u}$ to the

$^1A_{1g}$ state, we use TDDFT forces to obtain the optimized excited $^3T_{1u}$ geometry. We refer to the work by Jin et al.[60] for the implementation of the TDDFT method and the details of the TDDFT calculations on MgO. With the optimized $^3T_{1u}$ and $^1A_{1g}$ geometries at hand, the TDDFT excitation energies between the two states at both geometries are computed. We denote the TDDFT excitation energy from $^1A_{1g} \rightarrow^3 T_{1u}$ at the optimized geometry X by $E_{TDDFT}^{^1A_{1g}\rightarrow^3T_{1u}}@x$, where X can be either $^1A_{1g}$ or $^3T_{1u}$. The DMET VEE from $^1A_{1g}$ to $^3T_{1u}$ at the relaxed $^3T_{1u}$ structure (E_{DMET}^{em}) is calculated through the following equation:

$$E_{DMET}^{em} = E_{DMET}^{^1A_{1g}\rightarrow^3T_{1u}}@^1A_{1g} - \left[E_{TDDFT}^{^1A_{1g}\rightarrow^3T_{1u}}@^1A_{1g} - E_{TDDFT}^{^1A_{1g}\rightarrow^3T_{1u}}@^3T_{1u}\right] \quad (1)$$

$$= E_{DMET}^{^1A_{1g}\rightarrow^3T_{1u}}@^1A_{1g} - E_{TDDFT}^{corr} \quad (2)$$

where $E_{DMET}^{^1A_{1g}\rightarrow^3T_{1u}}@^1A_{1g}$ is the DMET non-embedding limit VEE, reported in the last two columns of Table 1. The last two terms in equation 1 have been combined into E_{TDDFT}^{corr}. This equation is used to calculate E_{DMET}^{em} for each supercell, the corresponding values for CAS-DMET and NEVPT2-DMET are mentioned in Table 2.

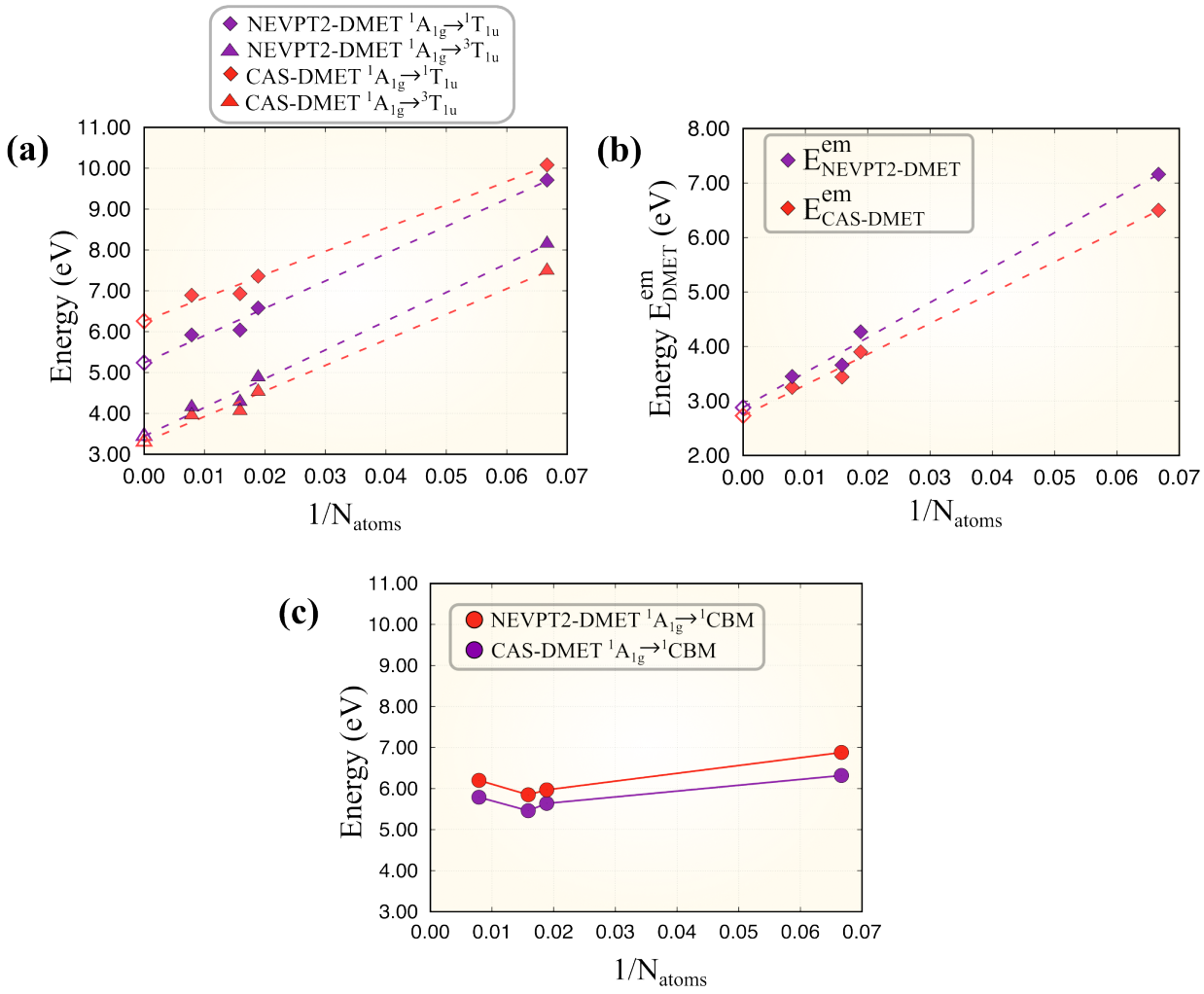

Figure 7: (a) The thermodynamic limit of the singlet-singlet and singlet-triplet defect localized transitions calculated through CAS-DMET and NEVPT2-DMET. The non-embedding limit energies are plotted as a function of the system size, i.e., the number of atoms (N_{atoms}). (b) The CAS-DMET and NEVPT2-DMET non-embedding limit photoionization energies plotted as a function of N_{atoms}.

Table 1: Convergence of the F^0-center excitation energies in MgO for increasing supercell sizes. TDL stands for the extrapolated thermodynamic limit estimate of the respective excitation energies, assuming a 1/N convergence. Here, N denotes the number of atoms in a supercell as a representative of the system size. All energies are in units of eV.

Supercell	CAS-DMET	NEVPT2-DMET	CAS-DMET	NEVPT2-DMET
	$^1A_{1g} \rightarrow {}^1T_{1u}$		$^1A_{1g} \rightarrow {}^3T_{1u}$	
Primitive $2 \times 2 \times 2$	10.08	9.71	7.49	8.15
Primitive $3 \times 3 \times 3$	7.36	6.58	4.53	4.88
Conventional $2 \times 2 \times 2$	6.93	6.04	4.06	4.28
Primitive $4 \times 4 \times 4$	6.89	5.79	3.95	4.15
TDL	6.26	5.24	3.40	3.44

To get a meaningful understanding in the context of solid-state systems, calculations must either be performed in or extrapolated to the thermodynamic limit (TDL), which is, for instance, the limit of an infinite number of atoms. There is, therefore, a critical need to get an insight into how the DMET excitation energies approach the thermodynamic limit with increasing system size. In our case, the $^1A_{1g} \rightarrow {}^1T_{1u}$, $^1A_{1g} \rightarrow {}^3T_{1u}$ and E^{em}_{DMET} defect localized transition energies decrease monotonically with supercell size and thus a linear extrapolation to the TDL is conveniently possible. The corresponding TDL plots for the first two transitions are shown in Figure 7 (a). The obtained values are summarized in Table 1. The NEVPT2-DMET value of 5.24 eV for the defect-localized singlet excitation energy is within 0.2-0.3 eV of the experimental value. The corresponding CAS-DMET value is 6.26 eV. The triplet excited state, at the ground state singlet optimized geometry, is thus more stable compared to the singlet by ≈1.8 eV. The TDL plot for DMET VEEs considering the relaxed excited state is shown in Figure 7(b) and the TDL values are mentioned in Table 2. If the relaxation of the excited triplet state is taken into account and photoemission occurs through $^3T_{1u} \rightarrow {}^1A_{1g}$, the corresponding energy should be approximated to the NEVPT2-DMET value of 2.89 eV. On the same note, for the photoionization process, when the non-embedding limits for each supercell are plotted as a function of supercell size, the excitation energy does not decrease monotonically (see Figure 7 (c)). The CAS-DMET and NEVPT2-DMET vertical excitation energy for primitive $4 \times 4 \times 4$ cell increases abruptly

and therefore a linear extrapolation to get the thermodynamic limit is not possible.

Table 2: F^0-center excitation energies for increasing supercell sizes after considering geometry relaxation of the excited $^3T_{1u}$ state. All energies are in units of eV.

Supercell	E^{corr}_{TDDFT}	$E^{em}_{CAS-DMET}$	$E^{em}_{NEVPT2-DMET}$
Primitive $2 \times 2 \times 2$	0.99	6.50	7.16
Primitive $3 \times 3 \times 3$	0.63	3.90	4.25
Conventional $2 \times 2 \times 2$	0.70	3.36	3.58
Primitive $4 \times 4 \times 4$	0.62	3.33	3.53
TDL		2.74	2.89

The optical absorption energies obtained by NEVPT2-DMET are in good agreement with those obtained from other quantum chemistry calculations, as summarized in Table 3. Our extrapolated NEVPT2-DMET value is in closer agreement with the experimental absorption energy compared to the CASPT2 cluster calculations[6] by around 0.2 eV and agrees within 0.04-0.06 eV with periodic equation of motion coupled cluster singles and doubles (EOM-CCSD) results.[62] An embedded-BSE study[12] showed that the transition momentum matrix elements from $A_{1g} \rightarrow T_{1u}$ transition are greater in magnitude than those of $A_{1g} \rightarrow CBM$, which implies that the transition to T_{1u} state is more probable than the photoionization. Our NEVPT2-DMET values again agree very well with their defect localized excitation value of 5.23 eV

For the emission energy corresponding to the de-excitation from the triplet excited state, EOM-CCSD[7] and CASPT2 cluster calculations[6] have been reported. The corresponding values by CAS-DMET (3.30 eV) and NEVPT2-DMET (3.44 eV) are within 0.25 eV of the EOM-CCSD value. However, these studies do not take into account the relaxed excited $^3T_{1u}$ state geometry. The GW-BSE[9] and QMC[8] reports compute the decay energies through the excited singlet T_{1u} state along the A_{1g} mode. The embedded-BSE results predict the photoemission to occur through a ionization process involving the CBM with a value of 2.93 eV. These emission energies are marked with an asterisk in Table 3 as they correspond to likely correspond to the emission band at 3.1 eV, with the decay mechanisms not involving the triplet defect localized excited state. The CAS-DMET and NEVPT2-DMET values,

2.74 eV and 2.89 eV respectively, accounting the relaxed excited state, are in much better agreement with the experimental photoemission signal at 2.4 eV compared to the various available literature values. Work is also in progress to directly compute DMET VEEs at relaxed excited state geometries.

Table 3: Reported optical transition energies in the F center in MgO. The experimental absorption energy is 5.03 eV and the emission occurs at 2.4 eV. All the energies are in units of eV.

Method	Absorption		Emission
	$^1A_{1g} \rightarrow {}^1T_{1u}$	$^1A_{1g} \rightarrow {}^1CBM$	$^3T_{1u} \rightarrow {}^1A_{1g}$
CAS-DMET@ROHF	6.26		2.74
NEVPT2-DMET@ROHF	5.24		2.89
CASPT2-cluster[6]	5.44		4.09
EE-EOM-CCSD[7]	5.28		3.66
Embedded-EOM-CCSD[62]	5.31		
Embedded-BSE@DDH[12]	5.23		2.93
G_0W_0@LDA-BSE[9]		4.95	3.40*
GW@PBE[10]		5.20	
QMC (FN-DMC)[8]		5.0	3.8*

Conclusion

We utilized multireference methods, specifically CASSCF and NEVPT2, along with density matrix embedding, to determine the electronic transition energies between the singlet ground state ($^1A_{1g}$) and singlet ($^1T_{1u}$), triplet ($^3T_{1u}$) defect localized excited states, within the bulk MgO's neutral oxygen vacancy. This is the first study in which a delocalized orbital corresponding to the CBM of g-symmetry was present in the active space. Our findings consistently support an optical transition involving the singlet defect localized states, and for this excitation, we observed linear trends as the DMET embedding space increases. By employing a two-step extrapolation scheme, we obtained a vertical excitation energy of 5.24 eV through NEVPT2-DMET, which can be interpreted as the absorption maxima. Employing the same procedure for the singlet-triplet defect localized excitation, both at the optimized ground state geometry and optimized excited state geometry, led to a NEVPT2-

DMET value of 2.89 eV for the later case. This value at the optimized excited state geometry is in good agreement with experiment, and overestimates the experimental emission value of 2.4 eV by approximately 0.5 eV. Our results suggest the observed emission to be originating from a $^3T_{1u}$ to $^1A_{1g}$ transition, motivating deeper investigation in this direction.

Acknowledgement

This material is based upon work supported by the U.S. Department of Energy, Office of Science, National Quantum Information Science Research Centers. M.R.H. and L.G. are partially supported by the U.S. DOE, Office of Basic Energy Sciences, Division of Chemical Sciences, Geosciences, and Biosciences under grant no. USDOE/DE-SC002183. The TDDFT work was supported by the computational materials science center Midwest Integrated Center for Computational Materials (MICCoM) for the implementation and use of spin-flip time-dependent density functional theory. We gratefully acknowledge the computing resources provided by the University of Chicago Research Computing Center.

Supporting Information Available

The basis set and active space details, procedure to vary the embedding subspace, excitation energies using different numbers of embedding orbitals for all the supercells and total energies are available in the Supporting Information.

References

(1) Vail, J. M. Theory of electronic defects: applications to MgO and alkali halides. *J. Phys. Chem. Solids* **1990**, *51*, 589–607.

(2) Pacchioni, G. Oxygen vacancy: the invisible agent on oxide surfaces. *ChemPhysChem* **2003**, *4*, 1041–1047.

(3) Giordano, L.; Pacchioni, G. Oxide films at the nanoscale: new structures, new functions, and new materials. *Acc. Chem. Res.* **2011**, *44*, 1244–1252.

(4) Ferrari, A. M.; Pacchioni, G. Electronic structure of F and V centers on the MgO surface. *J. Phys. Chem.* **1995**, *99*, 17010–17018.

(5) Illas, F.; Pacchioni, G. Optical properties of surface and bulk F centers in MgO from ab initio cluster model calculations. *J. Chem. Phys.* **1998**, *108*, 7835–7841.

(6) Sousa, C.; Illas, F. On the accurate prediction of the optical absorption energy of F-centers in MgO from explicitly correlated ab initio cluster model calculations. *J.Chem. Phys.* **2001**, *115*, 1435–1439.

(7) Gallo, A.; Hummel, F.; Irmler, A.; Grüneis, A. A periodic equation-of-motion coupled-cluster implementation applied to F-centers in alkaline earth oxides. *J. Chem. Phys.* **2021**, *154*, 064106.

(8) Ertekin, E.; Wagner, L. K.; Grossman, J. C. Point-defect optical transitions and thermal ionization energies from quantum Monte Carlo methods: Application to the F-center defect in MgO. *Phys. Rev. B* **2013**, *87*, 155210.

(9) Rinke, P.; Schleife, A.; Kioupakis, E.; Janotti, A.; Rödl, C.; Bechstedt, F.; Scheffler, M.; Van de Walle, C. G. First-principles optical spectra for F centers in MgO. *Phys. Rev. Lett.* **2012**, *108*, 126404.

(10) Tosoni, S.; Hevia, D. F.; Pena, J. P.; Illas, F. Prediction of optical properties of F centers in oxides from quasiparticle excitations. *Phys. Rev. B* **2012**, *85*, 115114.

(11) Chen, Y.; Williams, R.; Sibley, W. Defect cluster centers in MgO. *Phys. Rev.* **1969**, *182*, 960.

(12) Vorwerk, C.; Galli, G. Disentangling photoexcitation and photoluminescence processes in defective MgO. *Phys. Rev. Mater.* **2023**, *7*, 033801.

(13) Rosenblatt, G.; Rowe, M.; Williams Jr, G.; Williams, R.; Chen, Y. Luminescence of F and F+ centers in magnesium oxide. *Phys. Rev. B* **1989**, *39*, 10309.

(14) Henderson, B.; King, R.; Stoneham, A. The temperature dependence of the F band in magnesium oxide. *J. Phys. C: Solid State Phys.* **1968**, *1*, 586.

(15) Summers, G. P.; Wilson, T.; Jeffries, B.; Tohver, H.; Chen, Y.; Abraham, M. Luminescence from oxygen vacancies in MgO crystals thermochemically reduced at high temperatures. *Phys. Rev. B* **1983**, *27*, 1283.

(16) Hohenberg, P.; Kohn, W. Inhomogeneous electron gas. *Phys. Rev.* **1964**, *136*, B864.

(17) Perdew, J. P. Can Density Functional Theory Describe Strongly Correlated Electronic Systems? *Electron Correlations and Materials Properties 2* **2003**, 237–252.

(18) Hedin, L. New method for calculating the one-particle Green's function with application to the electron-gas problem. *Phys. Rev.* **1965**, *139*, A796.

(19) Sun, Q.; Chan, G. K.-L. Quantum embedding theories. *Acc. Chem. Res.* **2016**, *49*, 2705–2712.

(20) Mitra, A.; Pham, H. Q.; Pandharkar, R.; Hermes, M. R.; Gagliardi, L. Excited states of crystalline point defects with multireference density matrix embedding theory. *J. Phys. Chem. Lett.* **2021**, *12*, 11688–11694.

(21) Mitra, A.; Hermes, M. R.; Cho, M.; Agarawal, V.; Gagliardi, L. Periodic Density Matrix Embedding for CO Adsorption on the MgO(001) Surface. *J. Phys. Chem. Lett.* **2022**, *13*, 7483–7489.

(22) Haldar, S.; Mitra, A.; Hermes, M. R.; Gagliardi, L. Local Excitations of a Charged Nitrogen Vacancy in Diamond with Multireference Density Matrix Embedding Theory. *J. Phys. Chem. Lett.* **2023**, *14*, 4273–4280.

(23) Mitra, A.; Hermes, M. R.; Gagliardi, L. Density Matrix Embedding Using Multiconfiguration Pair-Density Functional Theory. *J. Chem. Theory Comput.* **2023**, *19*, 3498–3508.

(24) Jones, L. O.; Mosquera, M. A.; Schatz, G. C.; Ratner, M. A. Embedding methods for quantum chemistry: Applications from materials to life sciences. *J. Am. Chem. Soc.* **2020**, *142*, 3281–3295.

(25) Muechler, L.; Badrtdinov, D. I.; Hampel, A.; Cano, J.; Rösner, M.; Dreyer, C. E. Quantum embedding methods for correlated excited states of point defects: Case studies and challenges. *Phys. Rev. B* **2022**, *105*, 235104.

(26) Cortona, P. Self-consistently determined properties of solids without band-structure calculations. *Phys. Rev. B* **1991**, *44*, 8454.

(27) Wesolowski, T. A.; Warshel, A. Frozen density functional approach for ab initio calculations of solvated molecules. *J. Phys. Chem.* **1993**, *97*, 8050–8053.

(28) Jacob, C. R.; Neugebauer, J. Subsystem density-functional theory. *Wiley Interdiscip. Rev. Comput. Mol. Sci.* **2014**, *4*, 325–362.

(29) Libisch, F.; Huang, C.; Carter, E. A. Embedded correlated wavefunction schemes: Theory and applications. *Acc. Chem. Res.* **2014**, *47*, 2768–2775.

(30) Knizia, G.; Chan, G. K.-L. Density matrix embedding: A simple alternative to dynamical mean-field theory. *Phys. Rev. Lett.* **2012**, *109*, 186404.

(31) Wouters, S.; A. Jiménez-Hoyos, C.; KL Chan, G. *Fragmentation: Toward Accurate Calculations on Complex Molecular Systems*; John Wiley & Sons Ltd., 2017; Chapter 8, pp 227–243.

(32) Inglesfield, J. A method of embedding. *J. Phys. C: Solid State Phys.* **1981**, *14*, 3795.

(33) Zhu, T.; Cui, Z.-H.; Chan, G. K.-L. Efficient formulation of ab initio quantum embedding in periodic systems: Dynamical mean-field theory. *J. Chem. Theory Comput.* **2020**, *16*, 141–153.

(34) Zgid, D.; Chan, G. K.-L. Dynamical mean-field theory from a quantum chemical perspective. *J. Chem. Phys.* **2011**, *134*, 094115.

(35) Ma, H.; Sheng, N.; Govoni, M.; Galli, G. First-principles studies of strongly correlated states in defect spin qubits in diamond. *Phys. Chem. Chem. Phys.* **2020**, *22*, 25522–25527.

(36) Ma, H.; Sheng, N.; Govoni, M.; Galli, G. Quantum embedding theory for strongly correlated states in materials. *J. Chem. Theory Comput.* **2021**, *17*, 2116–2125.

(37) Vorwerk, C.; Sheng, N.; Govoni, M.; Huang, B.; Galli, G. Quantum embedding theories to simulate condensed systems on quantum computers. *Nat. Comput. Sci.* **2022**, *2*, 424–432.

(38) Pham, H. Q.; Hermes, M. R.; Gagliardi, L. Periodic electronic structure calculations with the density matrix embedding theory. *J. Chem. Theory Comput.* **2019**, *16*, 130–140.

(39) Cui, Z.-H.; Zhu, T.; Chan, G. K.-L. Efficient implementation of ab initio quantum embedding in periodic systems: Density matrix embedding theory. *J. Chem. Theory Comput.* **2020**, *16*, 119–129.

(40) Knizia, G.; Chan, G. K.-L. Density matrix embedding: A strong-coupling quantum embedding theory. *J. Chem. Theory Comput.* **2013**, *9*, 1428–1432.

(41) Booth, G. H.; Chan, G. K.-L. Spectral functions of strongly correlated extended systems via an exact quantum embedding. *Phys. Rev. B* **2015**, *91*, 155107.

(42) Wouters, S.; Jiménez-Hoyos, C. A.; Sun, Q.; Chan, G. K.-L. A practical guide to density matrix embedding theory in quantum chemistry. *J. Chem. Theory Comput.* **2016**, *12*, 2706–2719.

(43) Pham, H. Q.; Bernales, V.; Gagliardi, L. Can density matrix embedding theory with the complete activate space self-consistent field solver describe single and double bond breaking in molecular systems? *J. Chem. Theory Comput.* **2018**, *14*, 1960–1968.

(44) Hermes, M. R.; Gagliardi, L. Multiconfigurational self-consistent field theory with density matrix embedding: The localized active space self-consistent field method. *J. Chem. Theory Comput.* **2019**, *15*, 972–986.

(45) Scott, C. J.; Booth, G. H. Extending density matrix embedding: A static two-particle theory. *Phys. Rev. B* **2021**, *104*, 245114.

(46) Faulstich, F. M.; Kim, R.; Cui, Z.-H.; Wen, Z.; Kin-Lic Chan, G.; Lin, L. Pure State v-Representability of Density Matrix Embedding Theory. *J. Chem. Theory Comput.* **2022**, *18*, 851–864.

(47) Peschel, I. Entanglement in solvable many-particle models. *Braz. J. Phys.* **2012**, *42*, 267–291.

(48) Mitra, A. pDMET: A Code for Periodic DMET Calculations. 2022; `https://github.com/mitra054/mypDMET`, accessed Jan, 22, 2023.

(49) Pham, H. Q. pDMET: A Code for Periodic DMET Calculations. 2019; `https://github.com/hungpham2017/pDMET`, accessed Jan, 22, 2023.

(50) Sun, Q.; Berkelbach, T. C.; Blunt, N. S.; Booth, G. H.; Guo, S.; Li, Z.; Liu, J.; McClain, J. D.; Sayfutyarova, E. R.; Sharma, S.; Wouters, S.; Chan, G. K.-L. PySCF: The Python-Based Simulations of Chemistry Framework. *Wiley Interdiscip. Rev. Comput.* **2018**, *8*, e1340.

(51) Sun, Q. et al. Recent Developments in The PySCF Program Package. *J. Chem. Phys.* **2020**, *153*, 024109.

(52) Pizzi, G. et al. Wannier90 as A Community Code: New Features and Applications. *J. Phys.: Condens. Matter* **2020**, *32*, 165902.

(53) Pham, H. Q. pyWannier90: A Python Interface for wannier90. 2019; `https://github.com/hungpham2017/pyWannier90`, accessed Jan, 22, 2023.

(54) Giannozzi, P.; Baroni, S.; Bonini, N.; Calandra, M.; Car, R.; Cavazzoni, C.; Ceresoli, D.; Chiarotti, G. L.; Cococcioni, M.; Dabo, I., et al. QUANTUM ESPRESSO: a modular and open-source software project for quantum simulations of materials. *Journal of physics: Condensed matter* **2009**, *21*, 395502.

(55) Zhang, Q.; Tao, S.; Yi, R.; He, C.; Zhao, C.; Su, W.; Smogunov, A.; Dappe, Y. J.; Nichols, R. J.; Yang, L., et al. P. Giannozzi et al., Advanced capabilities for materials modelling with Quantum ESPRESSO. *J. Phys.: Condens. Matter* **2017**, *29*, 465901.

(56) Goedecker, S.; Teter, M.; Hutter, J. Separable dual-space Gaussian pseudopotentials. *Physical Review B* **1996**, *54*, 1703.

(57) Hartwigsen, C.; Gœdecker, S.; Hutter, J. Relativistic separable dual-space Gaussian pseudopotentials from H to Rn. *Phys. Rev. B* **1998**, *58*, 3641.

(58) Govoni, M.; Galli, G. Large scale GW calculations. *J. Chem. Theory Comput.* **2015**, *11*, 2680–2696.

(59) Yu, V. W.-z.; Govoni, M. GPU acceleration of large-scale full-frequency GW calculations. *J. Chem. Theory Comput.* **2022**, *18*, 4690–4707.

(60) Jin, Y.; Ju, V. W.-z.; Xu, A.; Govoni, M.; Galli, G. *In preparation* **2023**,

(61) Strand, J.; Chulkov, S. K.; Watkins, M. B.; Shluger, A. L. First principles calculations of optical properties for oxygen vacancies in binary metal oxides. *J. Chem. Phys.* **2019**, *150*, 044702.

(62) Lau, B. T.; Busemeyer, B.; Berkelbach, T. C. Optical properties of defects in solids via quantum embedding with good active space orbitals. *arXiv preprint arXiv:2301.09668* **2023**,

TOC Graphic